Residual stress control in large format polylactic acid additive manufacturing via fast thermomechanical simulation and in-operando imaging techniques

Rafaël Viano, Léo Demont, Pierre Margerit, Romain Mesnil, Jean-François Caron, Daniel Weisz-Patrault

Residual stress control in large format polylactic acid additive manufacturing via fast thermomechanical simulation and *in-operando* imaging techniques

Rafaël Viano[a,b,*], Léo Demont[d], Pierre Margerit[c], Romain Mesnil[b,d], Jean-François Caron[b], Daniel Weisz-Patrault[a,**]

[a]*LMS, CNRS, École Polytechnique, Institut Polytechnique de Paris, F-91128 Palaiseau, France*
[b]*Lab Navier, Univ Gustave Eiffel, ENPC, CNRS, F-77447 Marne la Vallée, France*
[c]*PIMM, CNRS UMR 8006, Arts et Métiers, F-75013 Paris, France*
[d]*Build'In, Marne la Vallée, France*

Abstract

Polymer-based Large Format Additive Manufacturing (LFAM) is an extrusion-based technology utilizing a robotic arm-mounted nozzle to deposit large-diameter polymer beads from heated polymer pellets. However, technical challenges arise due to slower cooling rates and heat accumulation, significant deformation that should be accounted for updating the nozzle path, as well as the development of residual stresses from thermo-chemical shrinkage leading to debonding. To overcome these challenges, the study proposes to combine recent and fast thermal and mechanical approaches. This computationally efficient digital twin of the process is validated experimentally on a thin-wall structure using polylactic acid as a feedstock material. To do so, anisotropic material properties are characterized, and *in-operando* temperature and displacement field measurements are performed using an infrared thermal camera and backward Digital Image Correlation techniques. Numerical results are in satisfying agreement with experimental data. The validated digital twin is then utilized to characterize the effect of process parameters on the number of layers above the glass transition temperature, the formation of residual stresses and the position offset between the top surface of the structure and the nozzle. This paper presents a fast numerical tool to better design fabrication conditions and improve the quality and fabricability of LFAM-produced parts.

Keywords: Large Format Additive Manufacturing ; Material Extrusion ; Fast Thermo-Mechanical Analysis ; Digital Twin ; Digital Image Correlation ; Infrared Thermal Imaging

1. Introduction

Additive Manufacturing (AM) encompasses a variety of distinct processes, all involving the progressive addition of material to form the part, and covering a wide range of materials (e.g., polymers, metal alloys, concretes, clays, ceramics or bio-materials) in various forms (e.g., filaments, wires, powders, or liquids). There are various techniques for processing these materials through different physico-chemical methods, including melting, binding, photopolymerization, and extrusion. Applications span multiple industries, including aerospace, automotive, naval, construction, and energy, where the demand for rapid prototyping and on-demand functional part production continues to grow [1, 2]. This paper focuses on Large Format Additive Manufacturing (LFAM) , which refers to manufacturing equipment capable of printing bulk structures exceeding one cubic meter in volume [3], using nozzle diameters greater than 2 millimeters. The acronym LFAM has been used for various classes of materials and technologies, including extrusion-based thermoplastics [4, 5], metal DED technologies [6], extrusion of concrete [7, 8] or geopolymers [9]. This paper more specifically focuses on polymer-based LFAM ,which is an extrusion-based technology that uses a nozzle mounted on a robotic arm for heating and stirring the feedstock material in the form of polymer pellets, which enables the deposition of large diameter beads of polymer at a temperature higher than the glass transition temperature. LFAM is dedicated to the fabrication of complex large-scale components while optimizing material performance and geometric flexibility. LFAM overcomes the size and design constraints typically associated with traditional manufacturing methods while minimizing material waste [10–12].

However, LFAM poses several technical challenges [3, 13]. First, due to the larger size of parts printed with LFAM, cooling rates are much slower than for conventional Fused Deposition Modeling (FDM) [14]. Indeed, heat loss is proportional to surface area while total heat is proportional to volume. This can lead to difficulties in stacking beads on top of each other, as stiffness of polymers is very low for temperatures higher than the glass transition temperature, resulting in significant deformation. In addition, the inherent orientation of LFAM leads to oriented microstructures, as the polymer chains tend to align with the printing direction [15]. Consequently,

*1st corresponding author e-mail: rafael.viano@enpc.fr
**2nd corresponding author e-mail: daniel.weisz-patrault@cnrs.fr

the material exhibits anisotropic behavior [16–18]. For instance, thermo-chemical shrinkage (i.e., due to temperature decrease and polymerization) is much higher in the bead section than in the printing direction, which should be quantified and taken into account in the printing strategy even though specific printing strategy can be used to compensate for anisotropy of the material [19]. Some studies therefore focused on the formulation of the printing material and its mechanical, thermal and rheological properties, to guarantee printability [20] and the selection of optimal process parameters. Material properties have also been studied under high pressure and temperature history [21], and during material transitions [22]. Mechanical and thermal properties are indeed crucial to control, as the predominant failure modes in printed structures are delamination, caused by weak interfaces, and warping.

Residual stress is also a major challenge for LFAM. Indeed, as the extruded material cools down, it undergoes thermo-chemical shrinkage leading to incompatible imposed strain between different layers and hence the buildup of interlayer residual stresses. In order to mitigate these effects and enhance the thermo-mechanical behavior, some studies characterize the impact of the addition of reinforcements, such as carbon or glass fibers, into the material [23–25]. Heat control strategy such as a heated substrate or infrared heating to elevate the surface temperature of the printed layer immediately before material deposition, can significantly enhance interlayer bonding [26]. Sustainability is reviewed with studies on the integration of recycled polymers and bio-derived materials in plastic-mix while maintaining manufacturability and performance [27, 28].

Most of the previously cited studies rely on design of experiments. While this approach is considered a standard practice, it remains both expensive and time-consuming. To overcome this difficulty, efficient thermo-mechanical simulations tracking temperature, displacement and stress evolution during the process should be developed, which could facilitate the optimization of process parameters and scanning strategies for each part geometry, ultimately reducing residual stresses and enhancing product quality. However, numerical simulation of LFAM (similarly as other AM processes) poses a significant challenge when it comes to carrying out parametric studies or optimization loops for the entire process. High computational costs are indeed often reported for conventional methods (e.g., fully coupled thermo-mechanical Finite Element Analysis (FEA) requiring very large number of degrees of freedom to accurately model the 3D part at the bead scale.

Typically, 3D FEA demands at least three to four elements across each direction of the bead section, which necessitates fine discretization along the tangential direction to prevent conditioning issues resulting in an extremely refined mesh for the entire 3D part [29]. For example, a multi-physics model for extrusion based concrete 3D-printing was recently proposed [30]. Computation cost being incompatible with parametric studies and optimization loops, contributions primarily focus on modeling parts after the design is finalized [31, 32], rather than serving as a design support tool.

To overcome this difficulty, numerical simulation tools have been developed to reach shorter computation cost. Common strategies rely on data-driven approaches for which datasets of comprehensive and computationally costly simulations of the process are used to derive a surrogate model. For instance Neural Network (NN) approaches have been used to create fast digital twins of the process [33–35], but are strongly limited by the large number of comprehensive simulations that should be included in the training dataset. To a lesser extent, the classical inherent strain method (ISM) (e.g., within the framework of metal AM [36–38]) may be classified as data-driven strategies because they rely on comprehensive reference simulations to obtain the so-called "inherent strain" that will be used in subsequent simplified and relatively fast elastic simulations. ISM though requires in general that new comprehensive reference simulations be carried out for different sets of process parameters. Furthermore, to directly reduce the computational cost of process simulations, several strategies have been developed. For instance, within the framework of metal AM, advanced meshing methods [39], including adaptive mesh refinement, parallel processing [40], and higher order discretization methods [41] have been proposed. Some analytical models have also been proposed to model specific process components, such as one that captures the complete extrusion dynamics in pellet based processes [42] or the warpage of parts [43].

A complementary and effective strategy is to weakly couple mechanical calculations with the computation of physically-based *imposed strains* (e.g., thermal expansion, phase transition etc.). This weak coupling strategy is especially effective if fast numerical methods are available for the thermal analysis and other related phenomena (e.g., phase transitions etc.) on the one hand, and for mechanical computations with imposed strains on the other hand. Indeed, since computing imposed strains involves solving complex physical processes with fine temporal and spatial discretization, separating these from stress and displacement calculations, which can be performed with coarser

resolution at the part scale, can significantly streamline the process [44, 45]. This weak coupling strategy allows for the use of fast, tailor-made models to compute the imposed strains before integrating them into the mechanical model. For example, within the framework of Direct Energy Deposition (DED), rapid thermal analysis and phase transition models named *ScanFast* have been developed [46, 47] and then used along with a mechanical model based on a 2D FEA following a weak coupling strategy to compute residual stresses and buckling [44].

But as already mentioned, the computational cost of mechanical simulations with imposed strains is also essential in the weak coupling strategy. To do so, a novel approach named *QuadWire* has recently been proposed and is dedicated to efficient mechanical computation of bead-based additive manufacturing (BBAM) (among which LFAM) [48]. The key contribution of *QuadWire* is that it reduces the total number of degrees of freedom by several orders of magnitude for large parts [49], without compromising accuracy or significantly limiting the level of detail achievable in numerical simulations. To do so, *QuadWire* is based on the concept of multi-particular materials initially introduced for multilayer composites [50, 51]. The aim and novelty of the present study are twofold.

(i) The fast thermal analysis *ScanFast* [46] and the mechanical model *QuadWire* [48] are used in a weak coupling strategy and experimentally validated for the first time in polymer-based LFAM. To do so, a set of experiments has been carried out in LFAM with Polylactic acid (PLA) as feedstock material. Anisotropic material properties have been characterized using various single bead experiments, and temperature and displacement fields have been measured during the process for a thin-walled structure using both a thermal camera and a visible-light camera coupled with backward Digital Image Correlation (DIC) techniques [44, 52]. Good agreement is observed between measured temperature and displacement fields and numerical results, which in turn provides an efficient digital twin of the process.

(ii) This validated digital twin is then used as a design tool so that the classical aforementioned challenges of LFAM (i.e., excessive deformation or residual stress inducing de-bonding with the substrate) can be analyzed and mitigated by modifying process parameters. In particular, this paper demonstrates that process parameters can be adjusted to limit the

formation of residual stresses while ensuring fabricability (i.e., reasonable displacements during fabrication).

The paper is organized as follows. Section 2 details the materials and methods, including the discussion of material selection, as well as the experimental setup and protocols. It also provides a concise overview of the theoretical background for DIC thermal modeling, and mechanical modeling. In section 2.5, the choice of reference frame for DIC is discussed and supported by experimental results obtained from monitoring a printed bead over 45 minutes. Section 3.2 utilizes bead experiments to identify material parameters for both the thermal and mechanical models, demonstrating good agreement between experimental and numerical results. Finally, section 3.3 validates our digital twin through wall experiments and further analysis.

2. Material and methods

2.1. Experiments

The material used in this study is PLA due to its compatibility with the experimental setup, favorable printing properties (i.e., extrudability and stable flow behavior) and accessibility. More specifically, *Nanovia* PLA pellets [53] loaded with 40% pine fibers were chosen to ensure sufficient contrast to perform accurate DIC. Table 1 presents the material properties of the selected PLA pellets provided by the manufacturer.

Table 1: Material properties of the pine fiber loaded PLA pellets: ρ is the density, ϕ is the volumetric concentration of pine fiber, T_g is the glass transition temperature and T_{ext} the extrusion temperature.

ρ [g.cm^{-1}]	ϕ [-]	T_{g} [K]	T_{ext} [K]
1.13	0.4	325	480–500

A LFAM equipment was installed in the *Build'In* robotic technological platform of the *École Nationale des Ponts et Chaussées*. It is composed of a single-screw *CEAD S25* pellet extruder installed on a track-mounted *ABB IRB 6620* six-axis robot arm. The extruder features four heat zones (max. 673 K), a maximum output of 25 kg/hr, and interchangeable nozzles ranging from 2

to 18 mm in diameter. Pellets are pneumatically conveyed from a *VISMEC Dryplus* pellet dryer, where pellets are dried at 323 K during at least 6 hours. To facilitate the separation of the part from the substrate, a smooth and non-adhesive 20 mm thick 1×0.5 m polypropylene (PP) board was chosen as build platform. A rigid aspiration table is used to anchor the build platform.

The displacement measurements are performed using a single high-resolution *Allied Vision Prosilica GT 5400* camera equipped with a *Sony IMX387* image sensor (max. 16.8 mega pixels at 7 frames per second), facing the printed wall at a distance of approximately 50 cm that allows to maximize the sensor coverage with the chosen 35 mm *Zeiss* lens. Two 50 W LED spotlights are added to the setup to provide constant lighting during the overall experiment duration. Temperature kinetics is recorded using an *Optris 400 thermal IR camera*. A schematic view of the experimental setup is presented in Figure 1. The emissivity of printed material is calibrated by placing sequentially two distinct printed structures (i.e., a thin wall and a single bead) in a *France Etuves XU980* furnace set to 320 K, 330 K, and 340 K for one hour each to ensure thermal equilibrium. A constant emissivity equal to one has been obtained and then used for the thermal camera.

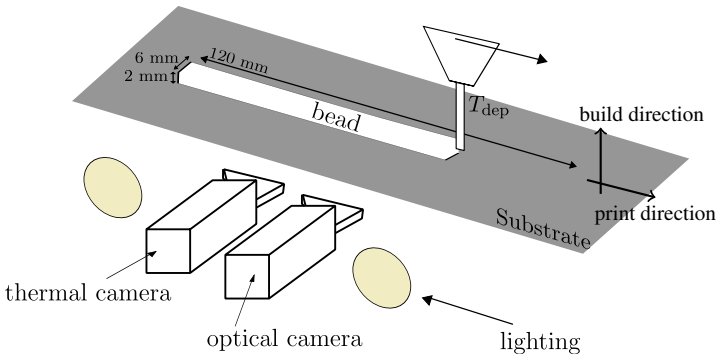

Figure 1: Schematic view of the LFAM process for a bead structure monitored by imaging techniques (optical and thermal)

The experimental plan first involves the printing of single beads to characterize material properties, and secondly involves the printing of a thin wall structure to validate the proposed digital twin. More precisely, a series of 120 mm long single beads were printed and monitored over 15 minutes to reach complete cooling. The bead length was chosen to capture large-scale deformation (size-effect) while maintaining sufficient image resolution. Each bead is cut using a cutter when de-

position is complete. In addition, a thin wall structure with dimensions $L = 120$ mm $\times H = 50$ mm was printed by depositing 25 successive beads on top of each others with a $\tau = 40$ seconds pause between each layer deposition. Considering the scanning speed $V = 16$ mm.s^{-1} each layer deposition takes 7.5 s. All process parameters for single beads and the thin wall structure are listed in Table 2. It should be noted that the feed rate is linearly associated with process parameters, especially the extruder rotation rate denoted by ω as demonstrated in Appendix A. The temperature of the material is controlled inside the extruder. The deposition temperature depends on the extruder rotation rate but is considered constant to first order.

Table 2: Process parameters: d is the nozzle diameter, h_d the deposition height, V the scanning speed, ω the extruder rotation rates and τ the interlayer dwell time.

d [mm]	h_d [mm]	V [mm.s^{-1}]	ω [rpm]	T_{ext} [K]	τ [s]
4	2	16	20, 30, 40	488	40

2.2. *Thermal analysis*

Temperature fields are simulated by using an adapted version of the fast thermal model proposed in [46] and improved in [44] and [47] named *ScanFast*. This approach is limited to single-track structures (i.e., arbitrary shaped multi-layer structures composed of a single bead of thickness) and relies on the assumption that heat flux in the printing direction is negligible compared to heat flux in the building direction. Short computation time is obtained by exploiting these assumptions and hence reducing the fully three-dimensional heat conduction problem into several independent two-dimensional multilayer structures. Within this framework, semi-analytical solution is derived for the multilayer heat conduction problem including convective heat losses with surrounding gas, heat exchange between the printed structure and the build platform, latent heat of fusion (and possibly latent heat of solid state phase transformations) and the heat brought by the heat source. It should be noted that since latent heat during polymerization is negligible, this contribution has been discarded in this contribution.

ScanFast has been validated for metals several times against experiments using laser powder-based DED: for 316L steel using infrared bi-chromatic pyrometer [46] and thermal camera [44], for 2507 duplex stainless steel using residual phase fractions (i.e., austgenite/ferrite) obtained by electron backscatter diffraction techniques, for 316L stainless steel using *in-operando* synchrotron X-ray diffraction techniques [45]. Nevertheless, there is no experimental validation of *ScanFast* for polymer based additive manufacturing, which is achieved in this contribution using LFAM with PLA as feedstock material.

As already mentioned, a weak coupling strategy is adopted in this paper so that the evolution of the temperature field is computed first using *ScanFast* and then used as input data (i.e., imposed strain) in a mechanical model of the process.

2.3. Mechanical model

The *QuadWire* mechanical model is a mechanical model designed for efficient simulations of BBAM processes. These processes encompass all the AM processes where elongated beads, undergoing significant eigenstrain, are successively added and assembled to form solid parts. The special feature of this model is that it is a multi-particular one-dimensional (i.e., wire) model containing four particles per material point. This modeling approach was selected to easily bound beads together (on top of each others and next to each others) by using kinematic relations between particles of different beads to create solid parts. Furthermore, a four particle modeling strategy enables to capture complex mechanical states, while significantly reducing computation time compared to conventional approaches. Indeed, using the classical three-dimensional *Cauchy* model requires at least three elements across the bead height and thickness, leading to very fine discretization in the printing direction to avoid conditioning issues and hence extensive computation time. On the contrary, since *QuadWire* is one-dimensional, cross-section dimensions are internal parameters, enabling a much coarser mesh in the printing direction without conditioning issues. Hence, despite enriched kinematics (with 12 degrees of freedom (DoF) per node since there are 4 particles), the total number of DoF is significantly reduced for large components compared to conventional approach [49].

The model is formulated using the principle of virtual power and within the framework of

standard generalized media. For more details on mathematical formulation the reader is referred to [48]. Numerical implementation is accessible in *Python* in the repository [54] with input data dedicated to FDM showing a drastic reduction in computation time (approximately 3 minutes on a laptop for *QuadWire*, while an equivalent conventional 3D computation using COMSOL Multiphysics is reported to take 3.7 hours in [34]).

In this contribution, material behavior is linear elastic under infinitesimal strain assumption and reads in matrix form:

$$\begin{cases} \boldsymbol{\Sigma} = \boldsymbol{R}^{\xi} \left(\boldsymbol{\xi} - \boldsymbol{\alpha}^{\xi} \Delta T \right) \\ \boldsymbol{M} = \boldsymbol{R}^{\chi} \boldsymbol{\chi} \end{cases} \tag{1}$$

Where $\boldsymbol{\Sigma}$ [N] and $\boldsymbol{M}$ [N.m] are generalized stress vectors with respectively 6 and 9 components, $\boldsymbol{\xi}$ is a generalized deformation vector with 6 components, $\boldsymbol{\alpha}^{\xi}$ is a 6 components thermal expansion vector, ΔT is the variation of temperature, $\boldsymbol{\chi}$ is a 9 components generalized curvature vector. Since *QuadWire* is an enriched one-dimensional model enabled to capture complex three-dimensional behavior of beads, there are a significant number of stiffness parameters involved in the linear elastic behavior. More precisely $\boldsymbol{R}^{\xi}$ and $\boldsymbol{R}^{\chi}$ are two symmetric stiffness matrices of size 6×6 and 9×9 respectively, which read:

$$R^{\xi} = \begin{pmatrix} p_1 & p_7 & p_8 & 0 & 0 & 0 \\ p_7 & p_2 & p_9 & 0 & 0 & 0 \\ p_8 & p_9 & p_3 & 0 & 0 & 0 \\ 0 & 0 & 0 & p_4 & 0 & 0 \\ 0 & 0 & 0 & 0 & p_5 & 0 \\ 0 & 0 & 0 & 0 & 0 & p_6 \end{pmatrix} \quad R^{\chi} = \begin{pmatrix} p_{10} & 0 & 0 & 0 & 0 & 0 & 0 & 0 & p_{21} \\ 0 & p_{11} & 0 & 0 & 0 & p_{19} & 0 & 0 & 0 \\ 0 & 0 & p_{12} & 0 & p_{20} & 0 & p_{22} & 0 & 0 \\ 0 & 0 & 0 & p_{13} & 0 & 0 & 0 & p_{23} & 0 \\ 0 & 0 & p_{20} & 0 & p_{14} & 0 & p_{24} & 0 & 0 \\ 0 & p_{19} & 0 & 0 & 0 & p_{15} & 0 & 0 & 0 \\ 0 & 0 & p_{22} & 0 & p_{24} & 0 & p_{16} & 0 & 0 \\ 0 & 0 & 0 & p_{23} & 0 & 0 & 0 & p_{17} & 0 \\ p_{21} & 0 & 0 & 0 & 0 & 0 & 0 & 0 & p_{18} \end{pmatrix} \tag{2}$$

Despite linearity, residual stresses develop due to the kinematic relations between successive beads and the temperature difference between the bead being deposited and the bead underneath.

2.4. *Backward digital image correlation*

DIC techniques are used to post-process images captured by the visible-light camera and obtain the evolution of marker positions and hence displacements during the process [55]. DIC procedures are based on the comparison of successive images of a structure. Given a reference image denoted by G and a current image denoted by g, the objective is to determine the displacement field denoted by $\boldsymbol{u}(\boldsymbol{X})$ that minimizes the differences between the two images (where $\boldsymbol{X} \in \mathcal{D}$ is the space variable and $\mathcal{D}$ is the Region of Interest (ROI)). A global DIC approach is used in this paper [56, 57]. In this approach, displacements are defined using FEA over a mesh covering the full ROI i.e. $\boldsymbol{u}(\boldsymbol{X}) = \boldsymbol{N}(\boldsymbol{X}).\{\boldsymbol{u}\}$ with $\boldsymbol{N}(\boldsymbol{X})$ representing the matrix of shape functions and $\{\boldsymbol{u}\}$ the nodal displacements to be determined.

However, for multi-layer structures, due to the additive nature of the studied process, the ROI in a conventional DIC procedure would be in constant evolution, that is to say that the correlation domain $\mathcal{D}$ would continuously grow as the process progresses. Consequently, the reference configuration of each material point would differ according to its deposition time. To overcome this issue, a single reference configuration is defined, by considering a backward DIC procedure where the reference configuration corresponds to the last image and is performed backwards in time. This technique was used for additive manufacturing in [44, 52]. All DIC results presented in this paper were obtained using an in-house academic code developed with *MATLAB* [58]. The meshing is performed using linear quadrangle elements. More theoretical background and implementation details are provided in Appendix B.

2.5. *Reference frame for DIC*

The reference frame is the frame from which displacements are computed. Displacements obtained by DIC therefore only capture mechanical evolution between the reference frame and the current frame, and the reference frame should be selected carefully to correctly analyze the deformation path. To do so, the evolution of a single bead at different times after the beginning of material deposition is presented in Figure 2. A red box represents the ROI tracked for DIC. The ROI significantly contracts in the vertical direction as long as deposition progresses, i.e between Figures 2 (a) and (c). In addition, as soon as the bead is cut from the nozzle such large and rapid

deformation stops (see. Figures 2 (c) and (d)). During deposition, thermochemical shrinkage and mechanical effects of the nozzle on the deposited bead take place. However, since the measured temperature in the ROI only decreases by around 30 K before the bead is cut, most of the very large deformation is attributed to the mechanical effect of the nozzle. Indeed, the deposition height h_d (i.e., the vertical distance between nozzle and build platform) is only 2 mm, whereas the feed rate results in an expansion of the bead to reach a thickness of around 2.2 mm. This expansion subsides as the nozzle moves further away, which explains the significant contraction observed between Figures 2 (a) and (c). However, during material deposition the measured temperature remains much higher than the glass transition temperature T_g, which is only reached after 1.9 min while the bead is cut from the nozzle before 11 s (see. Figure 2 (c)). Therefore the mechanical effect of the nozzle only induces negligible stress due to the very low stiffness of PLA at temperatures higher than T_g. As a result, for single beads, to correctly identify intrinsic material behavior, the reference frame for the DIC is chosen as the first image after the bead is cut from the nozzle, eliminating the nozzle's effect from the analysis.

In addition, for the thin wall structure, since the stress-free deformation caused by the nozzle is not considered in the proposed digital twin of the process, all images where the nozzle is still depositing the bead are removed from the analysis to make a fair comparison between DIC measurements and numerical results.

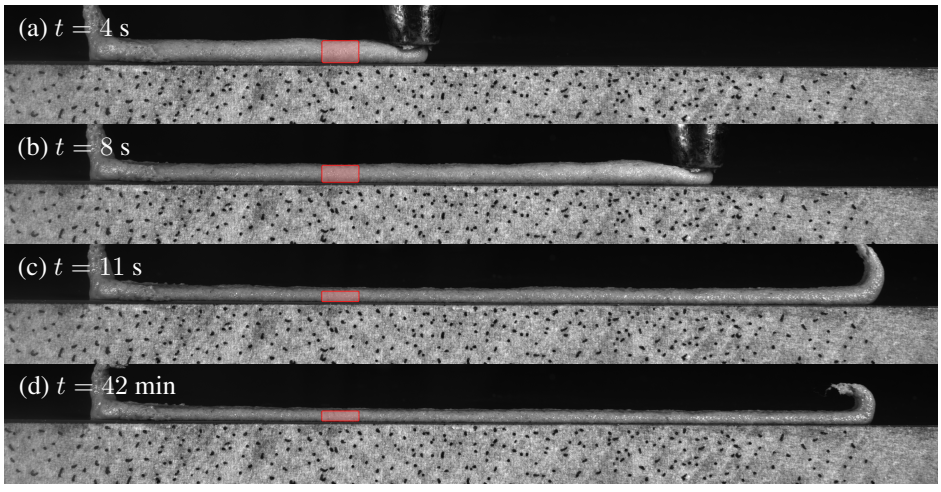

Figure 2: Evolution of a printed bead at different times t after beginning of material deposition : (a) $t = 4$ s, (b) $t = 8$ s, (c) $t = 11$ s, and (d) $t = 42$ min. The red box represents the ROI tracked throughout the process.

3. Results

3.1. Morphology of thin wall

The thin wall structure composed of 25 layers has been successfully fabricated without collapse as shown in Figure 3. After complete cooling, the bead height (i.e., build direction) is 2 mm and the bead thickness (i.e., transverse direction) is 6 mm similarly to single bead experiments. It should be noted that there is an excess of material at each end of the thin wall as well as geometric irregularities. In addition, during fabrication the thin wall gradually detached from the substrate on one side.

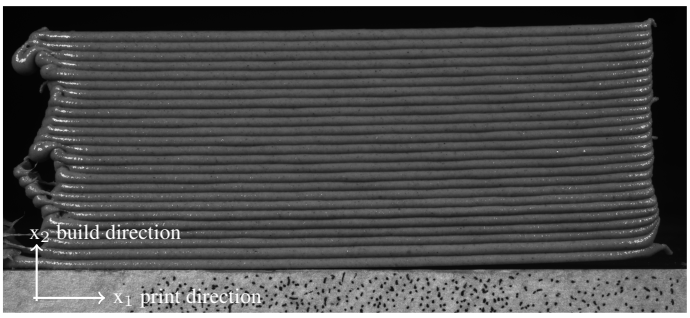

Figure 3: Thin wall after complete cooling.

3.2. Identification of material and modeling parameters

Thermal parameters. Since the feedstock material is composed of 40%.vol pine and 60%.vol PLA a simple mixture rule is applied to determine thermal properties. Thermal conductivity κ [W.m^{-1}.K^{-1}], density ρ [kg.m^{-3}], specific heat capacity c_p [J.g^{-1}.K^{-1}] are listed in Table 3. Temperature variation of the build platform is neglected and set to $T_{\text{sub}} = 295$ K as the build platform is very large in comparison to printed samples. The deposition temperature T_{dep} (i.e., the temperature of feedstock material wat nozzle outlet) is slightly lower than the extrusion temperature T_{ext} listed in Table 2, and is directly measured and set to $T_{\text{dep}} = 448$ K. The only two unknown and adjustable parameters are the heat transfer coefficient between the part and surrounding air denoted by H [W.m^{-2}.K^{-1}] and the heat transfer coefficient between the part and the build platform denoted

by H_{pla} [W.m^{-2}.K^{-1}]. For single bead experiments, temperatures have only been recorded after the layer is completed and cut from the nozzle. In addition, a single bead does not capture the complexity of thermal kinetics, therefore calibration is directly performed on the thin wall structure. Adjustable parameters that achieve the best fit between numerical and experimental temperature evolution and listed in Table 4.

Table 3: Thermal properties extracted from the literature.

	PLA	Pine
Thermal conductivity κ [W.m^{-1}.K^{-1}]	0.2	0.2
Density ρ [kg.m^{-3}]	1250	300
Specific heat capacity c_p [J.g^{-1}.K^{-1}]	1.59	1.76

Table 4: Calibrated parameters.

Heat transfer coefficient part/build platform H_{pla} [W.m^{-2}.K^{-1}]	60
Heat transfer coefficient part/air H [W.m^{-2}.K^{-1}]	23

Mechanical parameters. The mechanical tests presented in Appendix C were conducted on the single bead specimen to determine stiffness parameters of the printed material at room temperature. The Young's modulus and Poisson's ratio are respectively set to $E = 3.9$ GPa and $\nu = 0.32$. As detailed in [48] there are 24 stiffness components involved in *QuadWire*, which are identified by a minimization procedure consisting in fitting the Helmholtz free energy per unit length computed with *QuadWire* and the one obtained from a classical 3D FEA of a single bead under various loads. The minimization procedure is coded in *Python*. The 24 identified stiffness parameters denoted by $p_i^\dagger$ (with $1 \leq i \leq 24$) are listed in Tables 5 and 6 (where the symbol † means that the quantity has been optimized). In addition, the evolution of stiffness components as a function of temperature is implemented using a dimensionless activation function $f(T)$ where T is the temperature, so

Table 5: Optimized stiffness parameters $p_i^\dagger$ in [N] at room temperature.

$p_1^\dagger = 67.2$	$p_2^\dagger = 66.5$	$p_3^\dagger = 66.9$
$p_4^\dagger = 57.8$	$p_5^\dagger = 70.9$	$p_6^\dagger = 70.7$
$p_7^\dagger = 31.8$	$p_8^\dagger = 31.9$	$p_9^\dagger = 31.5$

Table 6: Optimized stiffness parameters $p_i^\dagger$ in [kN.mm^2] at room temperature.

$p_{10}^\dagger = 150.3$	$p_{11}^\dagger = 52.1$	$p_{12}^\dagger = 49.7$	$p_{13}^\dagger = 19.8$	$p_{14}^\dagger = 7.6$
$p_{15}^\dagger = 4.5$	$p_{16}^\dagger = 86.1$	$p_{17}^\dagger = 70.0$	$p_{18}^\dagger = 338.1$	$p_{19}^\dagger = 0.87$
$p_{20}^\dagger = 16.2$	$p_{21}^\dagger = 34.0$	$p_{22}^\dagger = 27.6$	$p_{23}^\dagger = 15.8$	$p_{24}^\dagger = 15.8$

that each stiffness component reads $p_i(T) = f(T)\, p_i^\dagger$ (with $1 \leq i \leq 24$). The chosen activation function is a sigmoid with transition temperatures $(T_1 + T_2)/2$:

$$f(T) = \epsilon + \frac{1+\epsilon}{1 + \exp\left[\eta\,(T - \frac{(T_1+T_2)}{2})\right]} \tag{3}$$

where $\epsilon = 10^{-9}$ is the lowest acceptable stifness and $\eta = 0.25$. Indeed, stiffness components rapidly tend to the optimized values at room temperature $p_i^\dagger$ for temperatures lower than T_2 and to $\epsilon \ll 1$ for temperatures above T_1. It should be noted that T_1, T_2 will be defined in the following as transition temperatures for polymerization (beginning and end temperature respectively).

Coefficients of thermo-chemical shrinkage during cooling are also determined by using single bead experiments. It should be noted that single beads are attached to the build platform but not strongly constrained in the build direction. Thermo-chemical shrinkage is therefore first analyzed in the build direction. Using DIC, the average strain component ε_{22} along the build direction is presented as a function of the average layer temperature in Figure 4 for the three tested conditions. The strain profiles as a function of temperature present three distinct nearly linear phases with different slopes. The threshold temperatures denoted by T_1 and T_2 correspond to beginning and end temperature of polymerization (where $T_2 \leq T_g \leq T_1$). Thermo-chemical shrinkage during

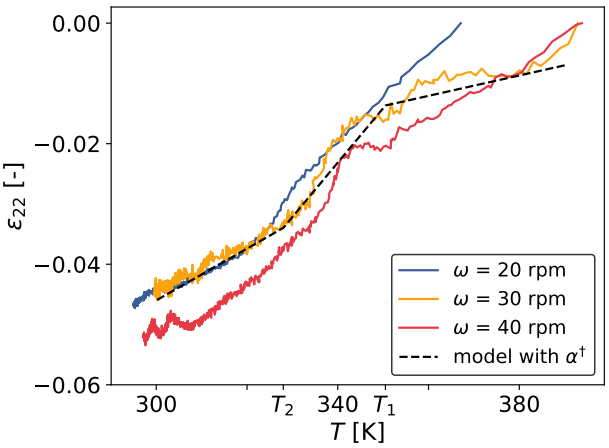

Figure 4: Average vertical strain component ε_{22} as a function of the average layer temperature for three different extruder rotation rates: $\omega = 20$ rpm (blue), $\omega = 30$ rpm (orange), $\omega = 40$ rpm (red). The dotted lines correspond to the optimized three slopes model.

cooling is modeled as the following equivalent thermal expansion coefficient:

$$\alpha(T) = \begin{cases} \alpha_1 & \text{if} \quad T > T_1 \\ \alpha_2 & \text{if} \quad T_2 < T \leq T_1 \\ \alpha_3 & \text{if} \quad T_2 \leq T \end{cases} \tag{4}$$

where $(\alpha_1,\ \alpha_2\ \alpha_3)$ are the values of the equivalent thermal expansion coefficients in the build direction. As already mentioned, polymer chains tend to align along the print direction which results in anisotropic thermo-chemical shrinkage. However, due to the clamped displacements on the build platform, the strain component along the print direction ε_{11} is two orders of magnitude lower than strain component along the build direction ε_{22}. It is therefore not possible to identify thermal expansion coefficient along the print direction by using single bead experiments. But by analyzing DIC results of the thin wall it has been found that the equivalent thermal expansion coefficient in the print direction is approximately a fifth of those in the build direction given in (4). However, it is not accurate to identify $(\alpha_1, \alpha_2\ \alpha_3)$ directly on Figure 4. Indeed, as already mentioned single beads are attached to the build platform and are therefore strongly constrained along the print direction, which induces Poisson's effect. As a result, the average bead strain in the build direction ε_{22} is slightly affected. Instead of directly identifying slopes on Figure 4, single beads experiments should be simulated using *QuadWire*, and the equivalent thermal expansion coefficients $(\alpha_1,\ \alpha_2$

α_3) along with transition temperatures (T_1, T_2) identified by numerical optimization in order to fit numerical results and measurements obtained by DIC and presented in figure 4. More precisely the following optimization problem is solved:

$$\begin{cases} (\alpha_1^\dagger, \alpha_2^\dagger, \alpha_3^\dagger, T_1^\dagger, T_2^\dagger) = & \operatorname{argmin} J(\alpha_1, \alpha_2, \alpha_3, T_1, T_2) \\ \text{s.t.} & \alpha_1, \alpha_2, \alpha_3 \geqslant 0 \text{ and } T_1 \geqslant T_g \geqslant T_2 \end{cases} \tag{5}$$

where the objective function J reads:

$$J(\alpha_1, \alpha_2, \alpha_3, T_1, T_2) = \frac{1}{2} \int_0^{t_f} \left(\varepsilon_{22}^{\mathrm{QW}}(t) - \varepsilon_{22}^{\mathrm{DIC}}(t) \right)^2 \mathrm{d}t \tag{6}$$

where $t_f = 15$ min is the duration of single bead experiments, $\varepsilon_{22}^{\mathrm{QW}}$ is a computed strain component obtained with *QuadWire* and $\varepsilon_{22}^{\mathrm{DIC}}$ is the corresponding strain component computed from experimental data using DIC. The optimization problem (5) is solved using a Nelson-Mead method. The three tested conditions (i.e., $w = 20, 30, 40$ rpm) are included in the optimization data set. Each single bead is discretized using $N_{\mathrm{e}} = 101$ elements in *QuadWire*. Boundary conditions consist in clamping bottom particles of the bead to the build platform. The thermal strain derived from the measured average temperature profile and thermal expansion coefficients (4) is imposed. The initial guess for the transition temperatures is set as the glass transition temperature ± 10 K, while the initial guess of equivalent thermal expansion coefficients are obtained through direct linear fitting of the on Figure 4. Eventually, the optimized thermal expansion coefficients $(\alpha_1^\dagger, \alpha_2^\dagger, \alpha_3^\dagger)$ and transition temperatures $(T_1^\dagger, T_2^\dagger)$ are computed and listed in Table 7.

Table 7: Optimized parameters $(\alpha_1^\dagger, \alpha_2^\dagger, \alpha_3^\dagger)$ in [K^{-1}] and $(T_1^\dagger, T_2^\dagger)$ [K]

$\alpha_1^\dagger = 1.7 \times 10^{-4}$	$\alpha_2^\dagger = 9.4 \times 10^{-4}$	$\alpha_3^\dagger = 4.0 \times 10^{-4}$	$T_1^\dagger = 350$	$T_2^\dagger = 328$

The optimized equivalent thermal expansion coefficients are not of the same order of magnitude as the typical values for cast PLA (i.e., around 4×10^{-5} K^{-1}), but are consistent with results obtained for printed PLA [15, 59] (where the authors studied the thermal expansion coefficient using DIC). The discrepancy with the cast PLA can be explained by the orientation of polymer chains in printed PLA. The strain component in the build direction ε_{22} is presented as a function of time

in Figure 5 for the three tested conditions (i.e., $\omega = 20, 30, 40$ rpm). Numerical results for initial and optimized equivalent thermal expansion coefficients are presented against measurements. The proposed identification procedure leads to a much better agreement between DIC measurements and numerical simulation.

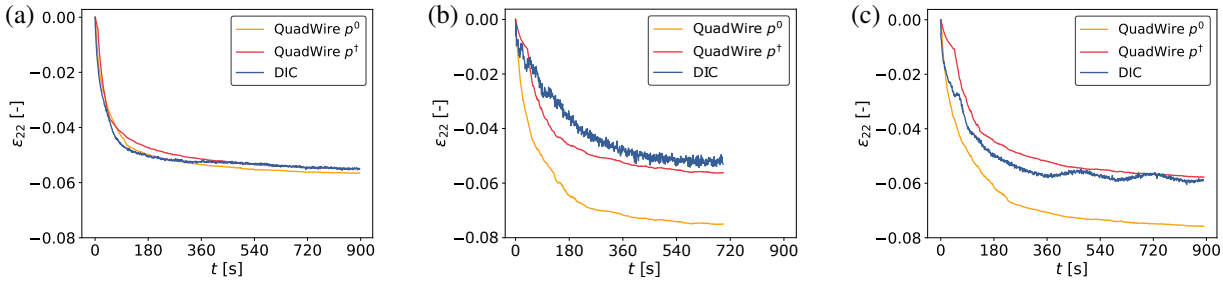

Figure 5: Evolution of the strain component ε_{22} for the three single bead experiments: (a) $\omega = 20$ rpm, (b) $\omega = 30$ rpm, and (c) $\omega = 40$ rpm with DIC (blue), initial guess parameters p^0 (orange), and optimized parameters $p^\dagger$ (red).

3.3. Digital twin validation

The combination of *ScanFast* and *QuadWire* creates a digital twin of the process. The experimental data obtained from thin wall structure are used to assess predictive capabilities of the proposed digital twin.

Thermal response. The simulated and measured temperature field after 22 layers depositions is presented in Figure 6. A good agreement is observed. It should be noted that specimen deformations are not considered in the thermal simulation so that a uniform and constant bead thickness of 6 mm and height of 2 mm are used. In addition, the temperature evolution of each layer is extracted from thermal images by selecting a single pixel at mid thickness of each cycle at $x_1 = -30$ mm where the thin-wall structure remains attached to the build platform during the entire fabrication. The obtained temperature evolution profiles are compared to the simulation in Figure 7, and a good agreement is observed. Therefore, *ScanFast* is validated for the tested condition using LFAM with PLA.

Mechanical response. Numerical results obtained with *QuadWire* are validated by comparing the final residual displacements at the end of cooling with measurements obtained with DIC.

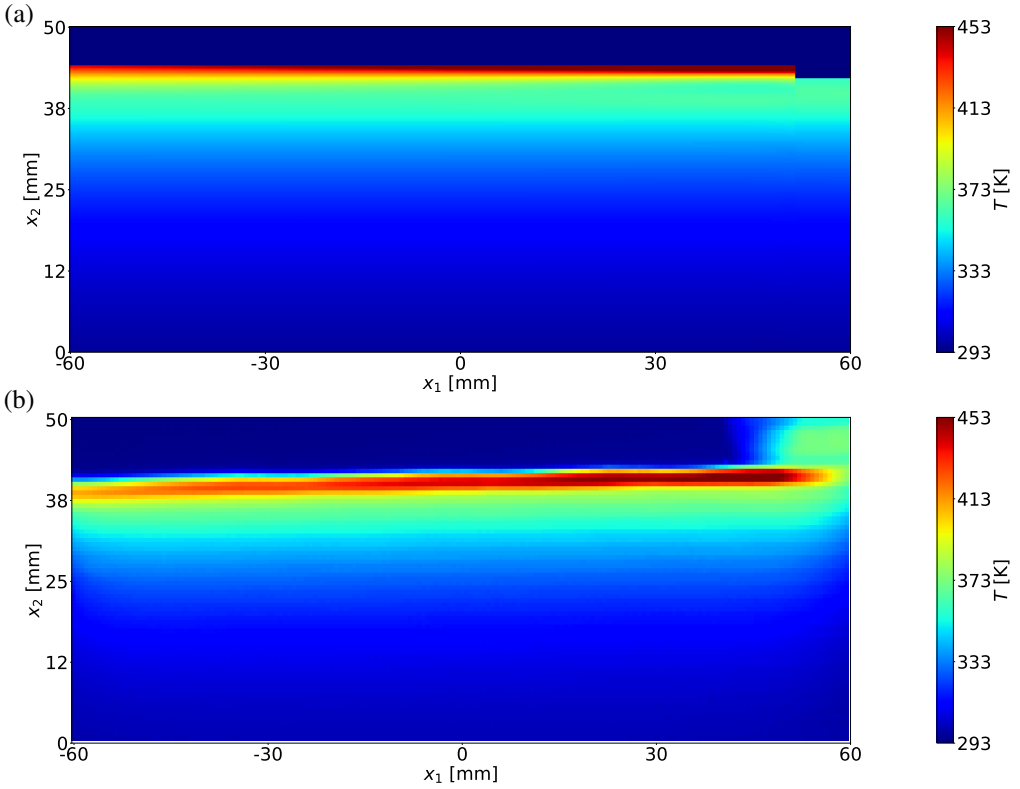

Figure 6: Temperature field after 22 layers depositions a) numerical results with *ScanFast*, b) measurements obtained using thermal camera.

Mechanical computations are carried out for the thin wall, with $N_{\mathrm{e}} = 20$ elements per layer. As already mentioned the thin wall warped and partially detached from the substrate during cooling. Such a fracture mechanism could be simulated by progressively breaking kinematic conditions between the bottom layer and the build platform. To do so, for each time step if in a given element the stress along the build direction σ_{22} reaches a certain threshold $\sigma_{22}^{\max}$, then the kinematic conditions are relaxed. Of course the threshold should be identified based on experimental data. However, to avoid technicalities, and since the proposed digital twin mostly aims at avoiding excessive deformation and residual stress (hence avoiding debonding), a simpler approach is followed for the purpose of validating *QuadWire*. Debonding is simply accounted for by only clamping displacements of particles that remain in contact with the build platform until complete cooling. Thus, there is no progressive debonding in the proposed simulation. In addition, the material excess at both ends of the thin wall is not considered in the numerical

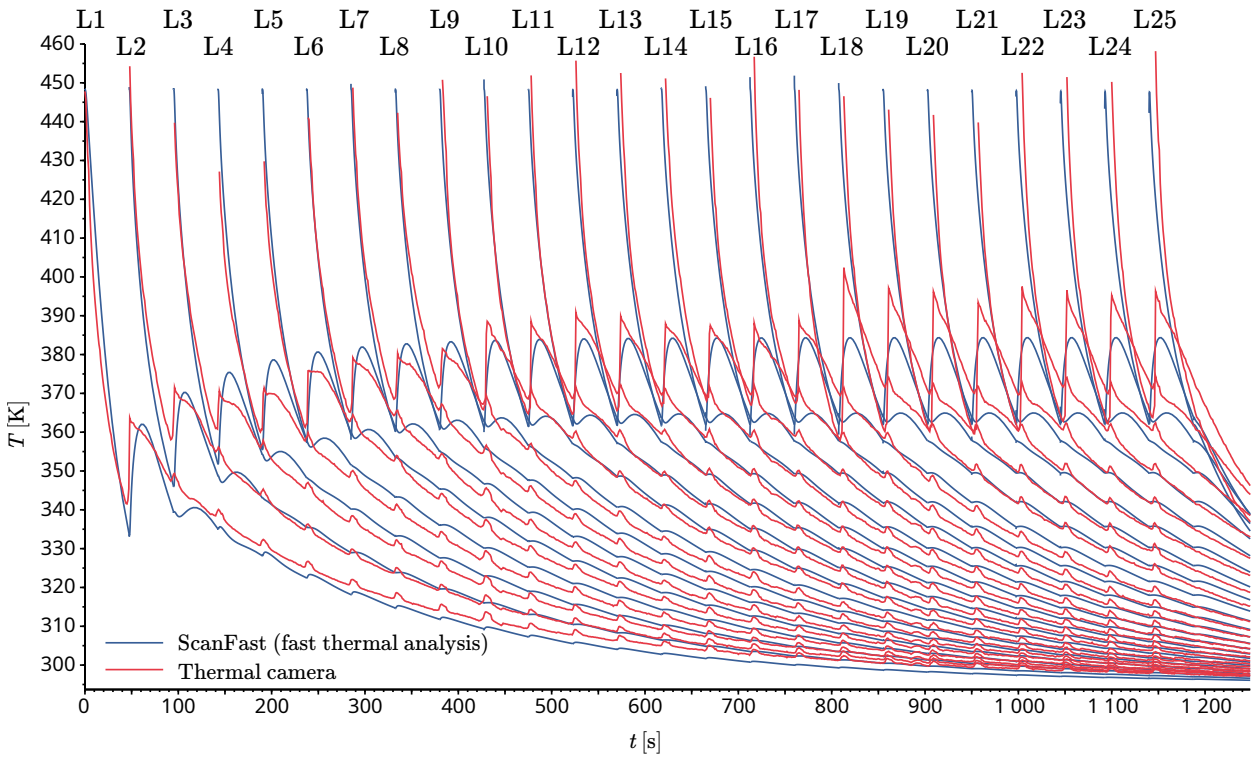

Figure 7: Simulated and measured temperature evolution of each layer (from Layer 1 (L1) to Layer 25 (L25)).

simulation. The temperature history of the entire thin wall structure is provided by *ScanFast*. Predicted and measured displacement fields denoted by u_1 and u_2 along print and build directions respectively are presented in Figure 8 after complete cooling. In addition, displacement profiles of three different layer (i.e., L1, L5 and L10) are presented in Figure 8. A satisfying, but not perfect, agreement is observed. Discrepancy is mostly attributed to the excess of material at both ends which locally creates additional stiffness. Nevertheless, the proposed digital twin demonstrates sufficient reliability to be used as a design tool to avoid excessive deformation or stress during fabrication.

4. Discussion

The proposed digital twin is now employed as a design tool to address common LFAM challenges such as (i) excessive number of layers stacked at temperatures above the glass transition, which could lead to the structure collapse due to the very low stiffness of PLA at high temperatures,

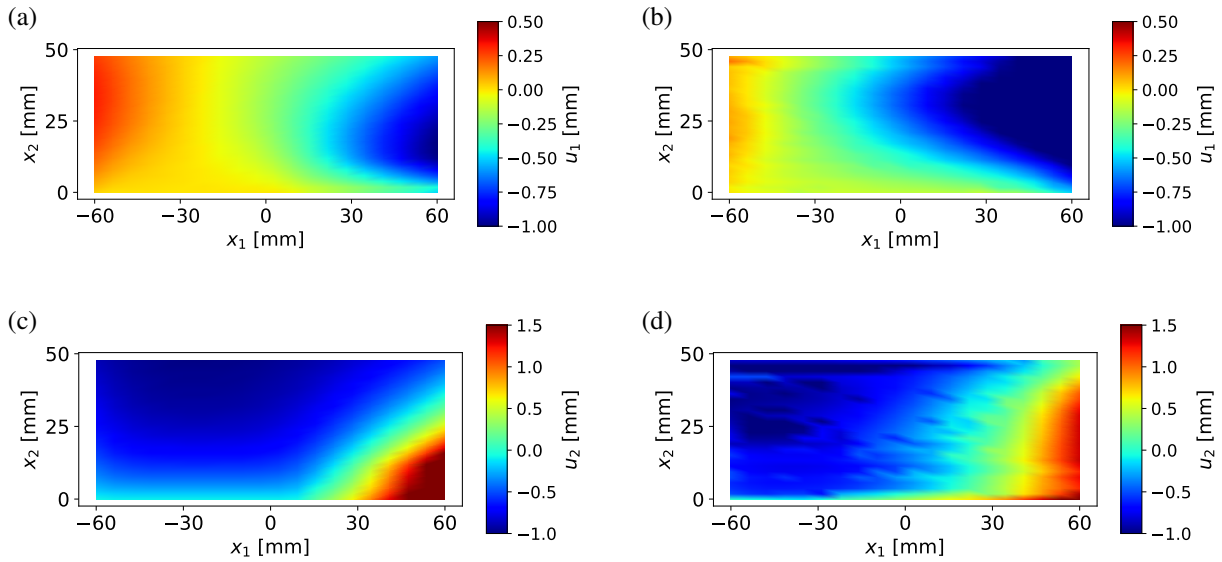

Figure 8: Displacement along the print direction u_1 (a, b) and displacement along the build direction u_2 (c, d) maps obtained with the digital twin (a, c) and with DIC measurements (b, d) across the thin-wall. The colorbar limits have been set to ensure better comparison between numerical and experimental maps.

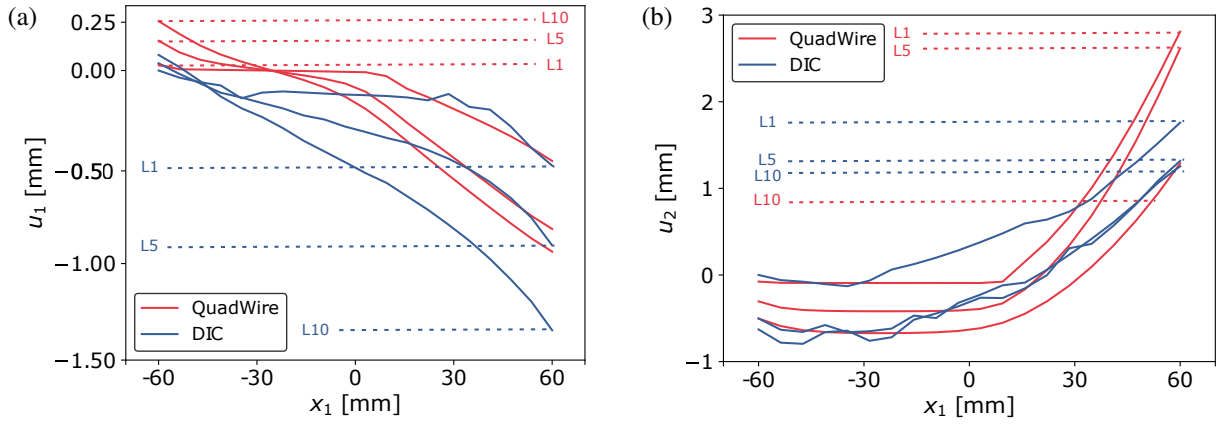

Figure 9: (a) Displacement along the print direction u_1 and (b) displacement along the build direction u_2 for the model (red) and DIC (blue) after complete cooling across different layers (L1: first layer, L5 : fifth layer, L10: tenth layer).

(ii) excessive stresses that could lead to substrate or interlayer debonding, and (iii) the adjustment of the nozzle path to accommodate progressive deformation of the structure.

One of the key experimental parameters for controlling the process is the interlayer dwell time, which directly influences temperature profiles, and consequently, the evolution of imposed strain as well as mechanical properties of layers during fabrication. To illustrate the influence of dwell

time, three different conditions are compared. All parameters are identical to those of the 25-layer thin-wall structure experiment, except for the interlayer dwell time: $\tau = 10$ s, $\tau = 40$ s, and $\tau = 180$ s. Contrary to the thin wall experiment debonding is not considered, hence displacements are clamped to the build platform along the entire length of the thin wall. Indeed, this setup reflects a defect-free experimental design scenario with perfect adhesion to the build platform, which is suitable for a design tool dedicated to avoid such defects.

Temperature profiles for the three tested conditions (i.e., $\tau = 10, 40, 180$ s) is presented in Figure 10. To compare thermal cycles of different durations a dimensionless time denoted by t^* has been introduced such as $t^* = t/(t_0 + \tau)$ where $t_0 = 7.5$ s is the duration of the layer deposition and τ the dwell time. Hence during deposition and dwell time of the i-th layer $i - 1 \leq t^* \leq i$. It is clearly observed that the dwell time significantly affects the cooling kinetics of the layers.

Lower dwell time is associated with higher heat accumulation. The risk of collapse due to excessive number of layer with very low stiffness is the first challenge identified for LFAM. For instance, there are around 5 layers whose temperature is higher than the glass transition temperature for the condition $\tau = 40$ s, while around 17 layers are above this temperature for the condition $\tau = 10$ s, and only 1 layer for the condition $\tau = 180$ s. Therefore, the proposed digital twin enables quantification of the number of stacked layers with very low stiffness for each set of process parameters, thereby addressing the risk of collapse

Temperature kinetics also affect the formation of residual stress and hence possible debonding, which is the second challenge identified for LFAM. The tensile and shear stresses in the build direction (i.e., σ_{22} and σ_{12}) are presented after complete cooling for the reference conditions (i.e., $\tau = 40$ s) in Figure 11. Similar color maps are obtained for other conditions (i.e., $\tau = 10, 180$ s). The most significant stresses are observed at both ends of the first few layers, which is due to the combined effect of clamping to the build platform and the edge effect at both sides of the thin wall. This observation is of particular interest, as it may result in debonding in modes I and II. Tensile and shear stresses (i.e., σ_{22} and σ_{12}) at the left edge (i.e., $x_1 = -60$ mm) of the first layer are presented in Figure 12 as a function of the dimensionless time t^*. Lower dwell time is associated with lower stress during deposition, which is due to the accumulation of layers with very low stiffness (i.e., temperature higher than the glass transition). This is favorable to prevent debonding

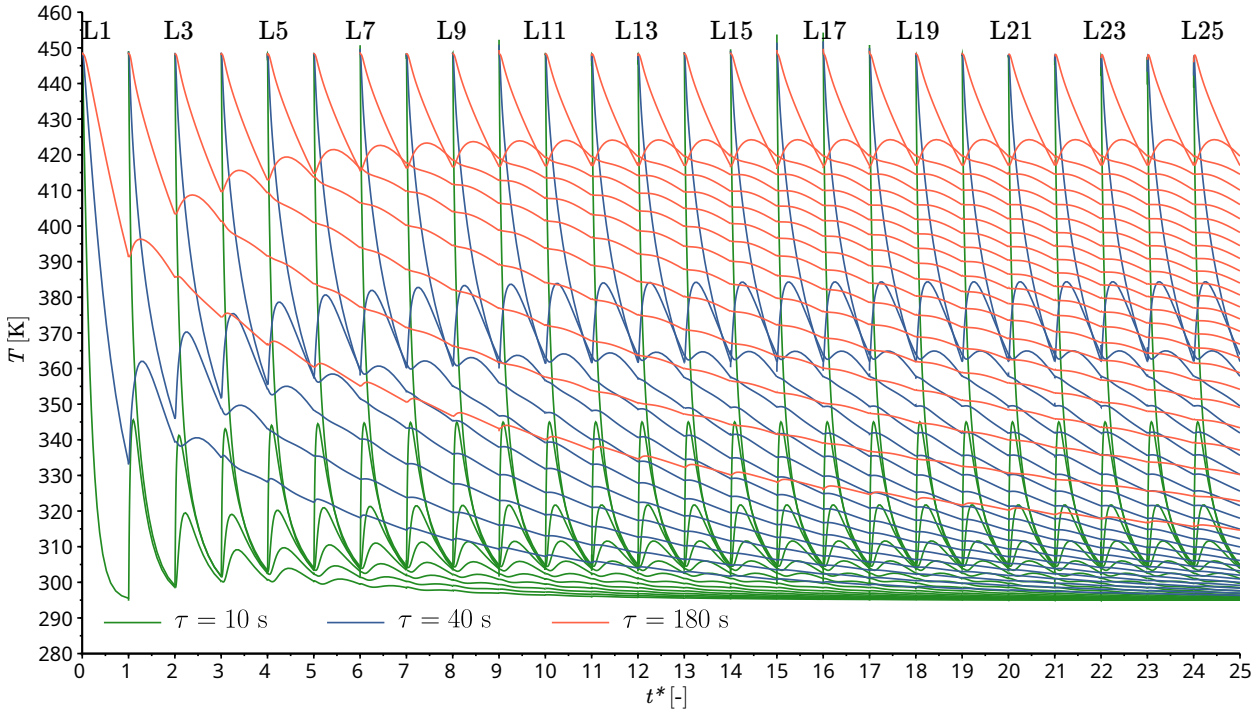

Figure 10: Simulated temperature evolution conditions of each layer (from Layer 1 (L1) to Layer 25 (L25)) for the three tested ($\tau = 10, 40, 180$ s). $t^* = t/(t_0 + \tau)$ where $t_0 = 7.5$ s is the duration of the layer deposition and τ the dwell time.

during fabrication. However, similar residual stresses develop after complete cooling even though higher dwell time is associated with higher residual stresses after complete cooling. This is due to the fact that higher dwell time is associated with higher temperature mismatch between the layer being deposited and the previous one. Therefore debonding may occur during the final cooling phase even for limited dwell times.

The last identified challenge of LFAM is the adjustment of the nozzle path to progressive deformation of the structure. Indeed, the position of the top surface of the thin wall structure does not necessarily evolve linearly during fabrication. The nozzle height should therefore be adjusted over time to ensure uniform deposition. For instance, assuming piece-wise constant deposition height (i.e., the nozzle height is $x_2 = i\, h_d$ for the i-th layer, where h_d is defined in Table 2), the position offset between the nozzle and the structure top surface denoted by Δx_2 [mm] is computed. To do so, even though the thin wall geometry is not updated at each time step of numerical simulations (i.e., infinitesimal strain assumption), the cumulative displacement can nevertheless

be computed to derive the top surface position as a function of time. It should be noted that if the deposited layers were not undergoing deformation, the position offset Δx_2 would vanish. Reciprocally, successive shrinkage of different layers corresponds to $\Delta x_2 < 0$. The position offset is presented in Figure 13 for the three tested conditions (i.e., $\tau = 10, 40, 180$ s). Longer dwell times are associated with more significant position offset. This is simply explained by the fact that each layer has time to shrink before the deposition of the next layer, which causes a lower top surface position and hence a larger position offset with the nozzle. For $\tau = 180$ s the position offset reaches more than 3 mm which would lead the deposited bead to drop by 3 mm before touching the top surface, which may induce instabilities. To avoid such issues, the proposed digital twin can be used to quantify the optimal nozzle path to maintain acceptable position offset during fabrication.

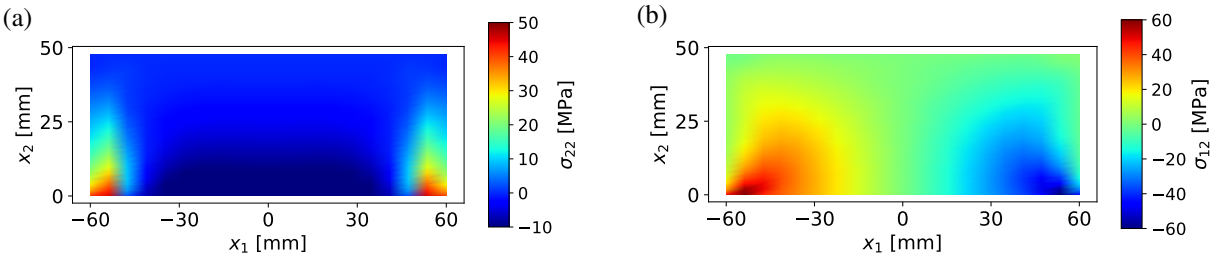

Figure 11: Tensile (a) and shear (b) stress maps in the build direction (σ_{22}, σ_{12}) for dwell time $\tau = 40$ s.

Another lever to reduce residual stresses and uncontrolled debonding during fabrication is the use of a heated build platform. To demonstrate the effect of this lever, a last condition is considered. The computation of the same thin wall structure is performed with controlled temperature of the build platform respectively set to $T_{\text{sub}} = 318$ K and dwell time $\tau = 40$ s. The computed temperature evolution of each layer is presented for both tested conditions with $\tau = 40$ s with $T_{\text{sub}} = 295$ K and $T_{\text{sub}} = 327$ K in Figure 14. Tensile and shear stresses (i.e., σ_{22} and σ_{12}) at the left edge (i.e., $x_2 = -60$ mm) of the first layer are presented in Figure 15 as a function of the dimensionless time t^* for the two build platform temperature conditions. Residual stresses at the end of fabrication are significantly reduced for when for the heated build platform as expected. Therefore the thin wall may be detached from the heated build platform and then cooled down without kinematic constrains.

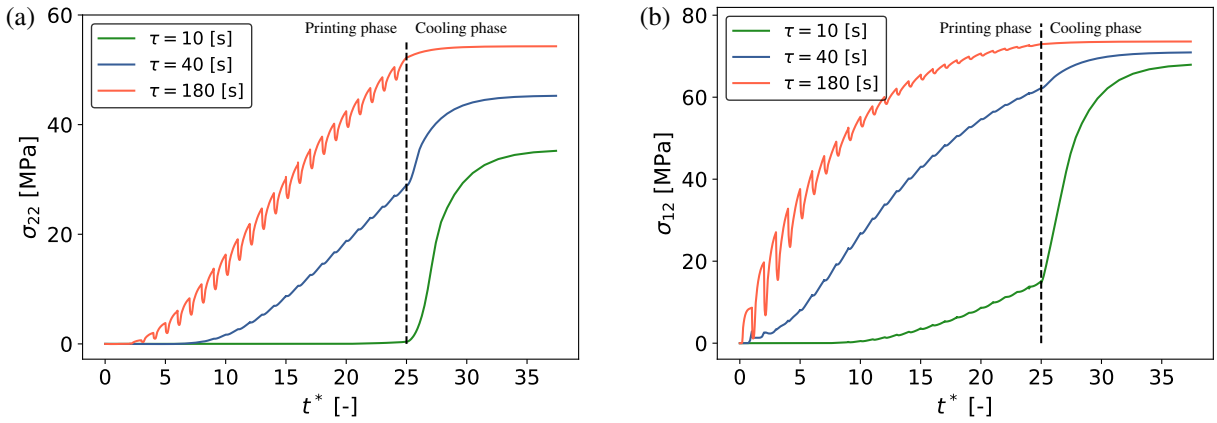

Figure 12: Time evolution of (a) tensile stress σ_{22} and (b) shear stress σ_{12} of the the left edge of the first layer ($x_1 = -60$ mm and $x_2 = 0$ mm) for dwell times $\tau = 10$ s (green), $\tau = 40$ s (blue), and $\tau = 180$ s (orange). $t^* = t/(t_0 + \tau)$ where $t_0 = 7.5$ s is the duration of the layer deposition and τ the dwell time. The vertical dotted lines marks the end of the wall deposition followed by a cooling phase until room temperature.

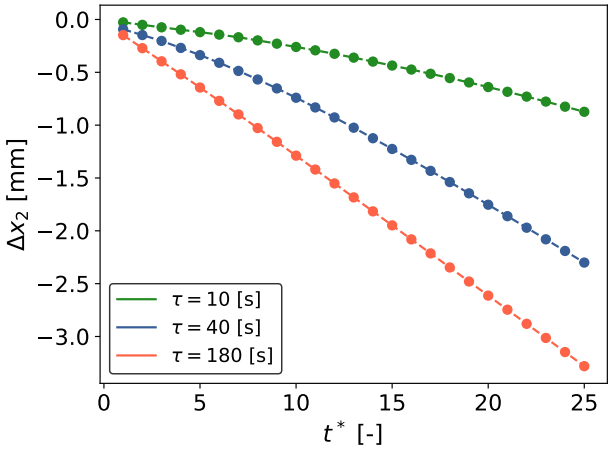

Figure 13: Time evolution of the position offset between the top surface of the thin-wall and the nozzle position for dwell times $\tau = 10$ s (green), $\tau = 40$ s (blue), and $\tau = 180$ s (orange) up to the end of printing. $t^* = t/(t_0 + \tau)$ where $t_0 = 7.5$ s is the duration of the layer deposition and τ the dwell time.

5. Conclusion

In this contribution, a computationally efficient digital twin of large format additive manufacturing has been proposed for polyactic acid (PLA) as feedstock material, and validated against experiments. To do so, single bead experiments have been performed to characterize anisotropic material properties. In addition, a 25 layers thin wall structure has been produced, and *in-operando*

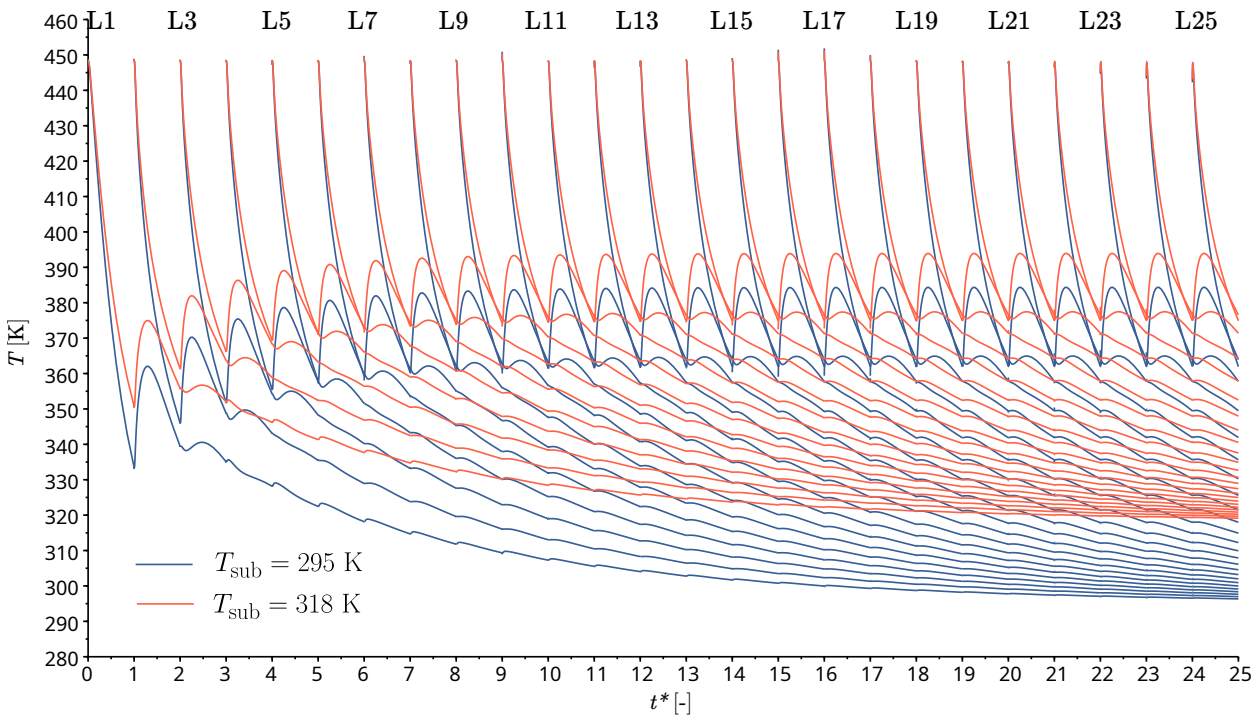

Figure 14: Simulated temperature evolution of each layer (from Layer 1 (L1) to Layer 25 (L25)) for $\tau = 40$ s and $T_{\text{sub}} = 295$ K (blue) and $T_{\text{sub}} = 318$ K (orange).

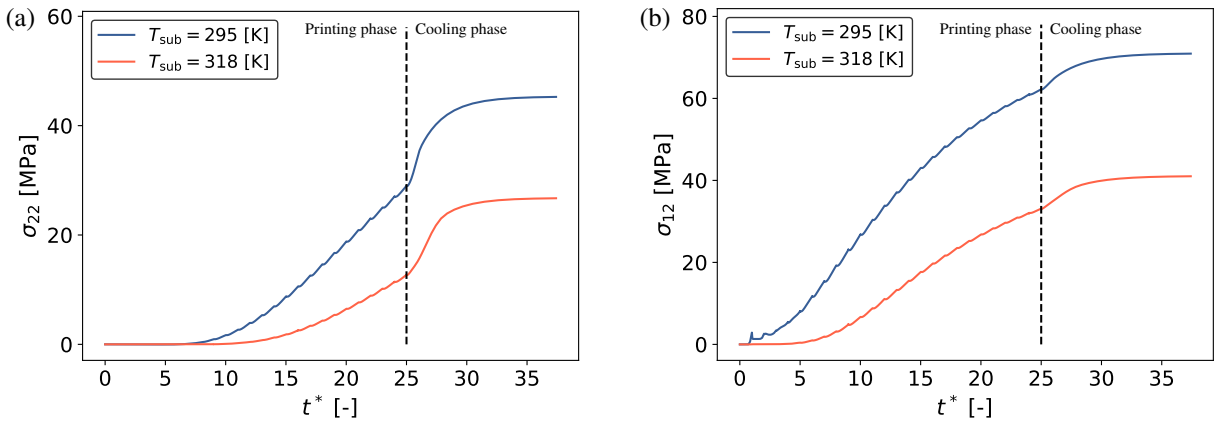

Figure 15: Time evolution of (a) tensile stress σ_{22} and (b) shear stress σ_{12} of the the left edge of the first layer ($x_1 = -60$ mm and $x_2 = 0$ mm) for build platform temperature $T_{\text{sub}} = 318$ K (blue) and $T_{\text{sub}} = 318$ K (orange). $t^* = t/(t_0 + \tau)$ where $t_0 = 7.5$ s is the duration of the layer deposition and τ the dwell time. The vertical dotted lines marks the end of the wall deposition followed by a cooling phase until room temperature.

temperature and displacement field measurements have been performed using an infrared thermal camera and backward digital image correlation techniques.

Once validated, the fast digital twin has been exploited as a design tool to address three major challenges of large format additive manufacturing: (i) the excessive number of layers stacked at temperatures above the glass transition, which could lead to the structure collapse due to the very low stiffness of PLA at high temperatures, (ii) excessive stresses that could lead to substrate or interlayer debonding, and (iii) the adjustment of the nozzle path to accommodate progressive deformation of the structure. In particular, the effects of dwell time and build platform temperature have been investigated. Numerical results demonstrate that the proposed fast digital twin enables comparing different printing strategies with respect to the three aforementioned challenges and hence offers an efficient tool to better design fabrication conditions and improve the quality and fabricability of LFAM-produced parts.

Appendix A. Material flow rate

The mass flow rate of the material was characterized as a function of process parameters, specifically the nozzle diameter and the extruder screw rotation speed. The extruder is positioned over a weighing scale and extrudes freely at a fixed screw rotation speed for 90 seconds. However, the material flow is not perfectly jet-like, and plastic droplets may form. To minimize their impact on the measurement, the operator cuts the extruded strand at the extruder outlet both at the beginning and end of the experiment. The test is repeated for different extruder screw rotation speeds and nozzle diameters.

The test results are shown in Figure A.16. Each point shows a test result which relates the extruder screw rotation speed [s^{-1}] with the measured flow rate [$g.s^{-1}$]. A linear regression model was applied to interpolate the experimental data for both nozzle diameters used. The linear trend is confirmed, as correlation coefficients exceed 0.995. The slope varies with the nozzle diameter, highlighting inertial effects present in the extruder screw. The larger the nozzle diameter, the higher the mass flow rate at a fixed rotation speed.

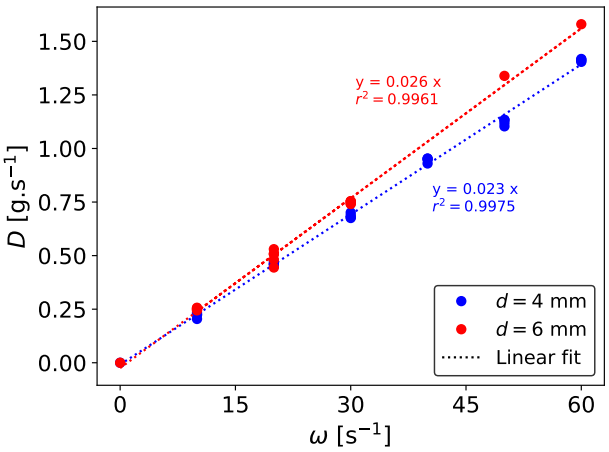

Figure A.16: Material flow rate D as a function of the extruder screw rotation speed ω for two different nozzle diameter: $d = 4$ mm (blue) and $d = 6$ mm (red). The circles represent the experimental data, while the dotted line shows the linear trend curve.

Appendix B. Digital Image Correlation

A theoretical background and implementation details related to the Digital Image Correlation methods used in the present work are explained.

Given a reference frame G and a current frame g, the DIC procedure consists in finding the transformation in between the two frames. The transformation is denoted by $\phi(\boldsymbol{X}, t) : \boldsymbol{X} \in \mathcal{D}_{t_f} \mapsto \boldsymbol{x} \in \mathcal{D}_t$ and is the solution of the following optimization problem :

$$\phi = \min_{\phi^*} \left[\int_{\mathcal{D}_{t_f}} [g(\phi^*(\boldsymbol{X}, t)) - G(\boldsymbol{X})]^2 \, \mathrm{d}\mathcal{D} \right] \tag{B.1}$$

where $\boldsymbol{X}$ denotes the reference configuration and $\boldsymbol{x}$ the actual configuration and $\mathcal{D}$ is the Region of Interest. The displacement $\boldsymbol{u}$ is discretized using a finite element mesh :

$$\boldsymbol{u} = \boldsymbol{N}(X).\{\boldsymbol{u}\} \tag{B.2}$$

where $\boldsymbol{N} : \mathcal{D} \mapsto \mathcal{R}^2$ denotes a set of piecewize-linear shape functions defined on the entire domain for the global approach and $\{\boldsymbol{u}\}$ is the nodal displacements. Hence, the transformation rewrites :

$$\phi(\boldsymbol{X}, t) = \boldsymbol{X} + \boldsymbol{N}(X).\{\boldsymbol{u}\} \tag{B.3}$$

The global approach enables to introduce a regularization of the ill-posed minimization problem using a Tikhonov method.

$$\phi = \min_{\phi^*} \left[\int_{\mathcal{D}_{t_f}} [g(\boldsymbol{X} + \boldsymbol{N}(\boldsymbol{X}).\{\boldsymbol{u}\}) - G(\boldsymbol{X})]^2 \, \mathrm{d}\mathcal{D} + \alpha \int_{\mathcal{D}_{t_f}} ||\nabla_{\boldsymbol{X}} \boldsymbol{B}(\boldsymbol{X}).\{\boldsymbol{u}\}||^2 \, \mathrm{d}\mathcal{D} \right] \tag{B.4}$$

where the $\boldsymbol{B}$ matrix is the first gradient of $\boldsymbol{N}$ so that $\boldsymbol{\varepsilon} = \boldsymbol{B}.\{\boldsymbol{u}\}$ and α is a regularization coefficient.

A Gauss-Newton algorithm is implemented to solve the minimization problem B.4 with an initial guess $\{\boldsymbol{u}^0\} = \boldsymbol{0}$. The parameter update is given by :

$$\{\boldsymbol{u}^{i+1}\} = \{\boldsymbol{u}^i\} - \boldsymbol{H}_i^{-1}.\boldsymbol{J}_i \tag{B.5}$$

where $\boldsymbol{J}$ and $\boldsymbol{H}$ are respectively the Jacobian and the pseudo-Hessian associated with the objective function. This procedure is repeated for each iteration until the norm of the displacement increment is small enough :

$$||\{\boldsymbol{u}^{i+1}\} - \{\boldsymbol{u}^i\}|| \leq \delta \tag{B.6}$$

where δ is a small fraction of a pixel.

Appendix C. Mechanical properties

Uniaxial tensile tests were performed at ambient temperature. Specimens measuring 10 cm in length with three different widths (5 mm, 15 mm, and 20 mm) were printed using different process parameters. The specimens were instrumented with *Kyowa* bidirectional strain gauges. The tensile tests were conducted using an *Instron 6022* testing machine. The test protocol involved a controlled strain cycle of tension-compression with a displacement speed of the movable crosshead set to $v = 5\,\mu\text{m.s}^{-1}$. The operator reversed the loading direction once the stress in the specimen exceeded a predefined limit of 5 MPa, ensuring that the material remained within the elastic regime.

The stress-strain curves presented in Figure C.17 presents the mechanical behavior of a specimen. The elastic regime is observed and maintained throughout the two loading cycles. The Young's moduli were determined by performing a linear fit of the experimental stress-strain curve, whereas the Poisson's ratio was determined by the ratio between the Young's moduli. The Young's

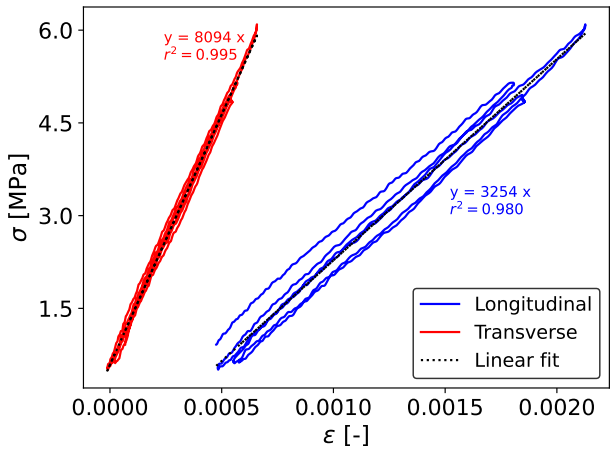

Figure C.17: Longitudinal (blue) and transverse (red) stress-strain (σ, ε) curve under uniaxial tensile tests. The dashed black lines are linear fits of the experimental data.

modulus of the material was identified in the direction of mechanical loading. Table C.8 presents the average and standard deviation of the Young's modulus E and Poisson's ratio ν for the tested specimens. These results align well with the expected order of magnitude for materials of this type.

Table C.8: Results of uniaxial tensile tests: average Young's modulus E and Poisson's ratio ν with standard deviations.

Parameter	**Average value**	**Standard deviation**
E [GPa]	3.9	0.32
ν [-]	0.32	0.04

References

[1] I. Gibson, D. W. Rosen, B. Stucker, M. Khorasani, D. Rosen, B. Stucker, M. Khorasani, Additive manufacturing technologies, volume 17, Springer, 2021.

[2] K. Kanishka, B. Acherjee, Revolutionizing manufacturing: A comprehensive overview of additive manufacturing processes, materials, developments, and challenges, Journal of Manufacturing Processes 107 (2023) 574–619.

[3] D. Moreno Nieto, S. I. Molina, Large-format fused deposition additive manufacturing: a review, Rapid Prototyping Journal 26 (2020) 793–799.

[4] D. M. Nieto, V. C. López, S. I. Molina, Large-format polymeric pellet-based additive manufacturing for the naval industry, Additive Manufacturing 23 (2018) 79–85.

[5] C. Ajinjeru, V. Kishore, P. Liu, J. Lindahl, A. A. Hassen, V. Kunc, B. Post, L. Love, C. Duty, Determination of melt processing conditions for high performance amorphous thermoplastics for large format additive manufacturing, Additive Manufacturing 21 (2018) 125–132.

[6] M. Borish, B. T. Gibson, C. Adkins, P. Mhatre, Automated process planning for embossing and functionally grading materials via site-specific control in large-format metal-based additive manufacturing, Materials 15 (2022) 4152.

[7] R. Robayo-Salazar, R. M. de Gutiérrez, M. A. Villaquirán-Caicedo, S. D. Arjona, 3d printing with cementitious materials: Challenges and opportunities for the construction sector, Automation in Construction 146 (2023) 104693.

[8] J.-F. Caron, L. Demont, N. Ducoulombier, R. Mesnil, 3d printing of mortar with continuous fibres: Principle, properties and potential for application, Automation in Construction 129 (2021) 103806.

[9] J. Archez, S. Maitenaz, L. Demont, M. Charrier, R. Mesnil, N. Texier-Mandoki, X. Bourbon, S. Rossignol, J.-F. Caron, Strategy to shape, on a half-meter scale, a geopolymer composite structure by additive manufacturing, Open Ceramics 5 (2021) 100071.

[10] F. Pignatelli, G. Percoco, An application-and market-oriented review on large format additive manufacturing, focusing on polymer pellet-based 3d printing, Progress in Additive Manufacturing 7 (2022) 1363–1377.

[11] C. M. Vicente, M. Sardinha, L. Reis, A. Ribeiro, M. Leite, Large-format additive manufacturing of polymer extrusion-based deposition systems: Review and applications, Progress in Additive Manufacturing 8 (2023) 1257–1280.

[12] D. Vanerio, M. Guagliano, S. Bagherifard, Emerging trends in large format additive manufacturing processes and hybrid techniques, Progress in Additive Manufacturing (2024) 1–28.

[13] J. Shah, B. Snider, T. Clarke, S. Kozutsky, M. Lacki, A. Hosseini, Large-scale 3d printers for additive manufacturing: design considerations and challenges, The International Journal of Advanced Manufacturing Technology 104 (2019) 3679–3693.

[14] J. Luo, Q. Luo, G. Zhang, Q. Li, G. Sun, On strain rate and temperature dependent mechanical properties and constitutive models for additively manufactured polylactic acid (pla) materials, Thin-Walled Structures 179 (2022) 109624.

[15] T. M. Corum, J. C. O'Connell, J. C. Brackett, A. A. Hassen, C. E. Duty, Measuring thermomechanical response of large-format printed polymer composite structures via digital image correlation, Additive Manufacturing 94 (2024) 104479.

[16] C. E. Duty, V. Kunc, B. Compton, B. Post, D. Erdman, R. Smith, R. Lind, P. Lloyd, L. Love, Structure and mechanical behavior of big area additive manufacturing (baam) materials, Rapid Prototyping Journal 23 (2017) 181–189.

[17] N. Zohdi, R. C. Yang, Material anisotropy in additively manufactured polymers and polymer composites: a

review, Polymers 13 (2021) 3368.

[18] P. B. Pintos, A. S. de León, S. I. Molina, Large format additive manufacturing of polyethylene terephthalate (pet) by material extrusion, Additive Manufacturing 79 (2024) 103908.

[19] C. Duty, J. Failla, S. Kim, J. Lindahl, B. Post, L. Love, V. Kunc, Reducing mechanical anisotropy in extrusion-based printed parts (2017).

[20] G. D. Goh, K. K. Wong, N. Tan, H. L. Seet, M. L. S. Nai, Large-format additive manufacturing of polymers: a review of fabrication processes, materials, and design, Virtual and Physical Prototyping 19 (2024) e2336160.

[21] L. Grassia, M. G. P. Carbone, G. Mensitieri, A. D'Amore, Modeling of density evolution of pla under ultra-high pressure/temperature histories, Polymer 52 (2011) 4011–4020.

[22] J. Brackett, Y. Yan, D. Cauthen, V. Kishore, J. Lindahl, T. Smith, Z. Sudbury, H. Ning, V. Kunc, C. Duty, Characterizing material transitions in large-scale additive manufacturing, Additive Manufacturing 38 (2021) 101750.

[23] V. Kunc, V. Kishore, X. Chen, C. Ajinjeru, C. Duty, A. A. Hassen, High performance poly (etherketoneketone)(PEKK) composite parts fabricated using Big Area Additive Manufacturing (BAAM) processes, Technical Report, Oak Ridge National Lab.(ORNL), Oak Ridge, TN (United States). Manufacturing . . . , 2016.

[24] K. M. M. Billah, F. A. Lorenzana, N. L. Martinez, R. B. Wicker, D. Espalin, Thermomechanical characterization of short carbon fiber and short glass fiber-reinforced abs used in large format additive manufacturing, Additive Manufacturing 35 (2020) 101299.

[25] A. B. Stefaniak, L. N. Bowers, S. B. Martin Jr, D. R. Hammond, J. E. Ham, J. Wells, A. R. Fortner, A. K. Knepp, S. du Preez, J. R. Pretty, et al., Large-format additive manufacturing and machining using high-melt-temperature polymers. part ii: characterization of particles and gases, ACS Chemical Health & Safety 28 (2021) 268–278.

[26] V. Kishore, C. Ajinjeru, A. Nycz, B. Post, J. Lindahl, V. Kunc, C. Duty, Infrared preheating to improve interlayer strength of big area additive manufacturing (baam) components, Additive Manufacturing 14 (2017) 7–12.

[27] X. Tian, T. Liu, Q. Wang, A. Dilmurat, D. Li, G. Ziegmann, Recycling and remanufacturing of 3d printed continuous carbon fiber reinforced pla composites, Journal of cleaner production 142 (2017) 1609–1618.

[28] A. L. Woern, D. J. Byard, R. B. Oakley, M. J. Fiedler, S. L. Snabes, J. M. Pearce, Fused particle fabrication 3-d printing: Recycled materials' optimization and mechanical properties, Materials 11 (2018) 1413.

[29] B. Brenken, E. Barocio, A. Favaloro, V. Kunc, R. B. Pipes, Development and validation of extrusion deposition additive manufacturing process simulations, Additive manufacturing 25 (2019) 218–226.

[30] M. Pierre, M. Samudio, S. Ghabezloo, P. Dangla, Modelling the poromechanical behaviour of class g cement paste: A multiphysics approach from early age to hardened state, Cement and Concrete Research 193 (2025) 107852.

[31] M. Talagani, S. DorMohammadi, R. Dutton, C. Godines, H. Baid, F. Abdi, V. Kunc, B. Compton, S. Simunovic, C. Duty, et al., Numerical simulation of big area additive manufacturing (3d printing) of a full size car, SAMPE

599 J 51 (2015) 27–36.
600 [32] P. Castelló-Pedrero, C. García-Gascón, J. A. García-Manrique, Multiscale numerical modeling of large-format
601 additive manufacturing processes using carbon fiber reinforced polymer for digital twin applications, International
602 Journal of Material Forming 17 (2024) 15.
603 [33] C. Liu, W. Tian, C. Kan, When ai meets additive manufacturing: Challenges and emerging opportunities for
604 human-centered products development, Journal of Manufacturing Systems 64 (2022) 648–656.
605 [34] Q. Zhu, K. Yu, H. Li, Q. Zhang, D. Tu, Rapid residual stress prediction and feedback control during fused
606 deposition modeling of pla, The International Journal of Advanced Manufacturing Technology (2022) 1–12.
607 [35] M. Hassan, M. Misra, G. W. Taylor, A. K. Mohanty, A review of ai for optimization of 3d printing of sustainable
608 polymers and composites, Composites Part C: Open Access (2024) 100513.
609 [36] Y. Ueda, K. Fukuda, M. Tanigawa, New measuring method of 3-dimensional residual stresses based on theory
610 of inherent strain, Journal of the Society of Naval Architects of Japan 1979 (1979) 203–211.
611 [37] N. Keller, V. Ploshikhin, New method for fast predictions on residual stress and distortion of am parts, in: 2014
612 International Solid Freeform Fabrication Symposium, University of Texas at Austin.
613 [38] X. Liang, L. Cheng, Q. Chen, Q. Yang, A. C. To, A modified method for estimating inherent strains from detailed
614 process simulation for fast residual distortion prediction of single-walled structures fabricated by directed energy
615 deposition, Additive Manufacturing 23 (2018) 471–486.
616 [39] P. Michaleris, Modeling metal deposition in heat transfer analyses of additive manufacturing processes, Finite
617 Elements in Analysis and Design 86 (2014) 51–60.
618 [40] E. Neiva, S. Badia, A. F. Martín, M. Chiumenti, A scalable parallel finite element framework for growing geome-
619 tries. application to metal additive manufacturing, International Journal for Numerical Methods in Engineering
620 119 (2019) 1098–1125.
621 [41] A. Özcan, S. Kollmannsberger, J. Jomo, E. Rank, Residual stresses in metal deposition modeling: discretizations
622 of higher order, Computers & Mathematics with Applications 78 (2019) 2247–2266.
623 [42] A. Pricci, M. D. de Tullio, G. Percoco, Analytical and numerical models of thermoplastics: a review aimed to
624 pellet extrusion-based additive manufacturing, Polymers 13 (2021) 3160.
625 [43] A. Armillotta, M. Bellotti, M. Cavallaro, Warpage of fdm parts: Experimental tests and analytic model, Robotics
626 and Computer-Integrated Manufacturing 50 (2018) 140–152.
627 [44] D. Weisz-Patrault, P. Margerit, A. Constantinescu, Residual stresses in thin walled-structures manufactured by
628 directed energy deposition: In-situ measurements, fast thermo-mechanical simulation and buckling, Additive
629 Manufacturing 56 (2022) 102903.
630 [45] S. Gaudez, D. Weisz-Patrault, K. A. Abdesselam, H. Gharbi, V. Honkimäki, S. van Petegem, M. V. Upadhyay,
631 On the accuracy of temperature estimates from in operando x-ray diffraction measurements during additive
632 manufacturing (2023).

[46] D. Weisz-Patrault, Fast simulation of temperature and phase transitions in directed energy deposition additive manufacturing, Additive Manufacturing 31 (2020) 100990.

[47] A. Edwards, D. Weisz-Patrault, E. Charkaluk, Analysis and fast modelling of microstructures in duplex stainless steel formed by directed energy deposition additive manufacturing, Additive Manufacturing 61 (2023) 103300.

[48] L. Preumont, R. Viano, D. Weisz-Patrault, P. Margerit, G. Allaire, Quadwire: An extended one dimensional model for efficient mechanical simulations of bead-based additive manufacturing processes, Computer Methods in Applied Mechanics and Engineering 427 (2024) 117010.

[49] L. Preumont, R. Viano, D. Weisz-Patrault, P. Margerit, G. Allaire, Modèle 1d enrichi pour le calcul mécanique rapide: approche multiparticulaire appliquée à la fabrication additive par dépôt de cordon, in: 16ème Colloque National en Calcul de Structures.

[50] A. Chabot, Analyse des efforts à l'interface entre les couches des matériaux composites à l'aide de modèles multiparticulaires de matériaux multicouches (M4), Ph.D. thesis, Ecole Nationale des Ponts et Chaussées, 1997.

[51] T. Naciri, A. Ehrlacher, A. Chabot, Interlaminar stress analysis with a new multiparticle modelization of multilayered materials (m4), Composites Science and Technology 58 (1998) 337–343.

[52] P. Margerit, D. Weisz-Patrault, K. Ravi-Chandar, A. Constantinescu, Tensile and ductile fracture properties of as-printed 316l stainless steel thin walls obtained by directed energy deposition, Additive Manufacturing 37 (2021) 101664.

[53] Nanovia PLA bois granules : 40 % vol. composite de pin : Nanovia, ????

[54] R. Viano, P. Margerit, L. Preumont, D. Weisz-Patrault, QuadWire-Elastic (https://doi.org/10.5281/zenodo.10822309), Zenodo, 2024.

[55] H. Schreier, J.-J. Orteu, M. A. Sutton, et al., Image correlation for shape, motion and deformation measurements: Basic concepts, theory and applications, volume 1, Springer, 2009.

[56] Y. Sun, J. H. L. Pang, C. K. Wong, F. Su, Finite element formulation for a digital image correlation method, Appl. Opt. 44 (2005) 7357–7363.

[57] G. Besnard, F. Hild, S. Roux, "finite-element" displacement fields analysis from digital images: application to portevin–le châtelier bands, Experimental mechanics 46 (2006) 789–803.

[58] P. Margerit, An open source matlab DIC app. written in laboratoire navier, ecole des ponts et chaussées, champs-sur-marne, france, 2018.

[59] A.-I. Botean, Thermal expansion coefficient determination of polylactic acid using digital image correlation, in: E3S Web of Conferences, volume 32, EDP Sciences, p. 01007.